Modifier field strength effects on densification behavior and mechanical properties of alkali aluminoborate glasses

Kacper Januchta, Mathieu Bauchy, Randall E. Youngman, Sylwester J. Rzoska, Michal Bockowski, and Morten M. Smedskjaer

Phys. Rev. Materials **1**, 063603 — Published 28 November 2017

DOI: 10.1103/PhysRevMaterials.1.063603

Modifier Field Strength Effects on Densification Behavior and Mechanical Properties of Alkali Aluminoborate Glasses

Kacper Januchta[1], Mathieu Bauchy[2], Randall E. Youngman[3], Sylwester J. Rzoska[4], Michal Bockowski[4], Morten M. Smedskjaer[1,*]

[1] *Department of Chemistry and Bioscience, Aalborg University, Aalborg, Denmark*

[2] *Department of Civil and Environmental Engineering, University of California, Los Angeles, USA*

[3] *Science and Technology Division, Corning Incorporated, Corning, USA*

[4] *Institute of High-Pressure Physics, Polish Academy of Sciences, Warsaw, Poland*

* Corresponding author. e-mail: mos@bio.aau.dk

Abstract: The constituents of oxide glasses are typically classified as network-formers, which form the rigid backbone of glasses, and network-modifiers, which tend to either charge-stabilize tetrahedral network formers or depolymerize the network. Although it is well known that the properties of glasses depend on their degree of polymerization, little is known about the role of the type of elements used as network-modifiers. Here, based on a series of aluminoborate glasses comprising varying alkali oxide modifiers, we show that the glasses' structural and mechanical properties are controlled by the field strength (ratio of charge to size) of the modifiers. Namely, we show that the stiffness, hardness, and toughness depend on a fine balance between the atomic bonding energy, the packing efficiency of the atoms, and the ability of the network to densify reversibly or irreversibly, with each of these features showing a different dependence on the modifier field strength. This opens a new degree of freedom in the optimization of glass properties.

Keywords: glasses, aluminoborate, field strength, indentation cracking, fracture toughness, self-adaptivity.

I. INTRODUCTION

Oxide glasses are well known to suffer from low practical strength due to the concentration of tensile stresses at the tips of surface flaws and the lack of a stable shearing mechanism capable of dissipating these stresses [1]. This leads to a brittle fracture at some critical stress intensity [2], although some extent of nanoscale ductility has been reported [3,4]. Limiting the tendency to form flaws at the surface, or to initiate cracks from such flaws, would result in improved mechanical performances. Compositional design of new glasses through topological engineering [5] is a promising approach for improving the mechanical properties, as glass compositions can be continuously varied with elements from most of the Periodic Table due to the lack of stoichiometry requirements [6]. Properties such as hardness, modulus, fracture toughness, as well as cracking pattern, vary significantly as a function of chemical composition [7–9], and thus inherent structure at the atomic scale. For example, amorphous silica, consisting of fully connected SiO_4 tetrahedral units, forms ring cracks originating at the surface [10,11] when subjected to sharp contact loading (i.e., indentation), as there are significant voids in its network that can facilitate densification, producing high radial tensile stresses at the contact boundary with the indenter [12]. However, upon addition of a modifying oxide (e.g. Na_2O), the interstices are filled with Na-cations, partly hindering densification and causing the material to deform more by shear flow [12], resulting in median/radial cracking [10]. A larger tendency to deform through shearing can also be obtained by pre-densifying the glass, which has recently been shown both experimentally and numerically [13–15]. The content of the network modifying oxide is also crucial for the mechanical response of other glassy frameworks such as borates [16], germanates [17], or mixed network-former glasses [18]. There is thus a large potential for improving mechanical properties such as hardness and toughness of oxide glasses by composition design [19–22]. For instance, we have recently demonstrated that highly damage-resistant aluminoborate glasses can be topologically engineered to exhibit a large extent of densification, which in turn is facilitated by large pressure-induced changes in the chemical environment of the network-forming cations (Al and B) [23,24]. However, to accelerate the search for stronger and more damage resistant glasses, there is a need to improve the current understanding of how different constituents influence the structure, and in turn the mechanical properties.

In this study, we investigate the nature of network-modifier type on glass mechanical properties by considering a series of five alkali aluminoborate glasses containing Cs_2O, Rb_2O, K_2O, Na_2O, or Li_2O. We study aluminoborate networks due to the limited understanding of mechanical properties in this system, and due to the ease of probing the structural changes of the network-forming Al and B atoms by solid state nuclear magnetic resonance (NMR) spectroscopy. The compositions in this work have fixed Al_2O_3, B_2O_3, and alkali oxide contents, and since all glasses contain monovalent alkali cations, the modifiers should exhibit similar roles in the aluminoborate network, i.e., serve to charge-balance tetrahedral AlO_4 and BO_4 units. However, due to the difference in the alkali size, their ability to charge-balance differs, as the same charge is distributed over a larger area for larger cations. This is conveniently quantified by the modifier field strength (*FS*), as defined by Dietzel [25].

$$FS = \frac{z_{alkali}}{(r_{alkali}+r_{oxygen})^2}, \quad (1)$$

where *z* and *r* are the charge and the ionic radius, respectively. Higher *FS* modifier cations are known to form stronger bonds with oxygen [26], which should result in higher hardness and modulus [7,27,28]. It has also been found that increasing the *FS* of the modifier yields a higher indentation fracture toughness [29,30], but the underlying structural origin of this behavior is not yet fully understood. Here, we report on the effect of substituting the alkali oxide type on hardness, elastic moduli, toughness, and extent of indentation cracking in an aluminoborate glass, in order to clarify the role of the modifier *FS* in controlling the mechanics of crack-resistant glasses. We compare the trends in mechanical properties with the glasses' tendency to densify when subjected to i) isostatic compression at elevated temperature (hot compression) and ii) localized indentation-induced densification at room temperature. The correlations between *FS* and mechanical properties are discussed using the structural information obtained from ^{11}B and ^{27}Al magic angle spinning (MAS) NMR spectroscopy experiments. As such, this study helps to facilitate the design of new glass materials with tailored mechanical performances. In future work, we will investigate aluminoborate glasses with divalent alkaline earth modifier cations to check the generality of the observed trends in mechanical properties with *FS*.

II. EXPERIMENTAL SECTION

II.A Sample Preparation. The nominal glass compositions introduced in this study are in the $25M_2O$-$20Al_2O_3$-$55B_2O_3$ system with M = K, Rb, and Cs. The preparation procedures for glasses with M = Na and Li are described elsewhere [23,24]. The glasses with M = K, Rb, and Cs were prepared by mixing appropriate amounts of the precursors (K_2CO_3, Rb_2CO_3, Cs_2CO_3, Al_2O_3, and H_3BO_3), and melting them in Pt-Rh crucibles at 1200-1300 °C depending on the composition. The final melts were quenched onto a brass plate and annealed around their glass transition temperature (T_g) estimated from the data for Li- and Na-aluminoborate glasses [23,24]. The chemical compositions were determined through flame emission and inductively coupled plasma optical emission spectroscopy techniques (Table 1).

The T_g values were determined using differential scanning calorimetry (DSC) measurements (DSC 449C, Netzsch) from the intercept between the extrapolated isobaric heat capacity of the glass (C_p) and the tangent to the inflection point recorded during the glass transition for 40 mg specimens with a specific thermal history (obtained by controlled cooling in the DSC at 10 K/min). C_p vs. T curves were acquired from a sapphire-calibrated energy output from the DSC. Each bulk glass specimen was then annealed at its measured T_g for 1 h, and cooled at 3 K/min. The glasses were confirmed to be amorphous using X-ray diffraction (Empyrean XRD, PANalytical) on powdered samples.

Samples of all glasses were cut into desired dimensions (~$15\times15\times3$ mm^3) for density, indentation, and hot compression experiments [31]. The high pressure treatment was carried out for all studied compositions by maintaining the specimens at their respective T_g in an N_2-atmosphere at 1.0 GPa for 30 min, and quenching from those conditions with an initial cooling rate of approx. 60 K/min. The high pressure setup is described in detail elsewhere [31].

II.B NMR spectroscopy. Na-, K-, Rb-, and Cs-glasses were subjected to ^{11}B and ^{27}Al MAS NMR experiments, while the results for the Li-glass are taken from Ref. [24]. Spectra were acquired with commercial spectrometers (VNMRs, Agilent) and 3.2mm MAS NMR probes (Agilent), using external magnetic field of 16.4 T. The detailed experimental procedures can be found in Ref. [24]. Fitting of ^{27}Al MAS NMR spectra to extract Al-speciation for each of the glasses was performed using DMFit [32] and the

CzSimple model, accounting for distributions in the quadrupolar coupling constant. Q MAS ½ and Gaus/Lor functions were used for fitting of ^{11}B MAS NMR spectra, also with DMFit.

II.C Density. Density (ρ) was determined for both the as-prepared and the compressed glass specimens using the Archimedes' principle of buoyancy with ethanol as the immersion fluid. Each specimen, weighing at least 1 g, was weighed in air and in liquid, ten times each, and the density was calculated as

$$\rho_{glass} = \frac{m_{air}}{(m_{air} - m_{liquid})}\left(\rho_{liquid} - \rho_{air}\right) + \rho_{air}. \quad (2)$$

Plastic compressibility (β), i.e., the permanent increase in density, is determined from the initial and final density values and the applied pressure (P) value,

$$\beta = \frac{\rho_{final} - \rho_{initial}}{\rho_{initial} \cdot P}. \quad (3)$$

II.D Indentation. All as-prepared and compressed specimens for indentation analyses were ground using SiC adhesive discs, and polished in water-free diamond suspensions to avoid hydration of the surface. Microindentation measurements (Duramin 5 microindenter, Struers) were performed using the Vickers type geometry at ambient temperature and relative humidity of 44±4%. Thirty identical indentations at 19.6 N press load and 10 s holding time were performed for each specimen. Cracks emanating from the corners of the indents were counted and their length from the center of the indents (c) was measured approximately 1 min after unloading. Vickers hardness (H_V) was calculated from the applied load (P in N) and the average half-length of the diagonals (a in μm) measured on the residual imprint visible under the optical microscope attached to the microindenter,

$$H_V = \frac{1854.4 \cdot P}{a^2}. \quad (4)$$

In addition, ten indents loaded at 245 mN were subjected to an analysis of the deformation mechanism, as suggested in Ref. [33]. An atomic force microscope (AFM, Ntegra, NT-MDT) was utilized to determine the topography of each indent both before and after a 2 h annealing cycle at $0.9T_g$ (temperature in K). Silicon tip cantilevers (NSG10, NT-MDT) were used in semi-contact mode to record 20×20 μm^2 or 25×25 μm^2 images at ~0.5 Hz scanning frequency. The acquired images with a 256×256 pixel resolution were then used to determine the indentation and pile-up volumes (V_i^- and V_i^+, respectively) for the initial indent, and the

corresponding volumes after thermal relaxation (V_a^- and V_a^+). The extent of densification is then quantified through the volume recovery ratio (V_R), which corresponds to the fraction of the indentation volume V_i^- that is due to densification. V_R is calculated as in Ref. [33],

$$V_R = \frac{(V_i^- - V_a^-) + (V_a^+ - V_i^+)}{V_i^-}. \quad (5)$$

In order to probe the glasses' elastic response to indentation, a Nano Indenter XP (MTS) equipped with a Berkovich geometry diamond tip was used to record at least ten loading-unloading cycles for a subset of the specimens. The applied load (P) and the displacement (h) were continuously monitored during the loading, the 10 s hold, and the unloading segments of each measurement cycle. The target d was 2000 nm. According to the Oliver-Pharr methodology [34], hardness (H_{nano}) was assessed from the projected contact area (A_c) of the indent (Eq. (6)), and the reduced indentation modulus (E_r) was calculated from the top 1/3 of the unloading P,h curve (Eq. (7)). Indentation modulus (E_{IT}) was then calculated from E_r and the elastic properties of the indenter material, i.e., diamond (Eq. (8)).

$$H_{nano} = \frac{P}{A_c}, \quad (6)$$

$$E_r = \frac{1}{2}\frac{dP}{dh}\sqrt{\frac{\pi}{A_c}}, \quad (7)$$

$$E_{IT} = \left(\frac{1}{E_r} - \frac{1-\nu_{ind}^2}{E_{ind}}\right)^{-1}. \quad (8)$$

In Eq. (7), dP/dh corresponds to the material stiffness recorded during unloading of the indenter. In Eq. (8), ν_{ind} and E_{ind} correspond to ν and E of diamond.

II.E Elastic moduli. An ultrasonic thickness gauge (38DL Plus, Olympus) was used to acquire the longitudinal and transverse wave velocities (V_L and V_T, respectively) in the glass specimens using the pulse-echo method. The thickness of the samples was measured with a digital micrometer. 20 MHz delay line transducers were used to induce the longitudinal and transverse waves. Shear modulus (G), Young's modulus (E), and Poisson's ratio (ν) were calculated using the density of the glass specimens according to Eqs. (9)-(11).

$$G = \rho V_T^2 \quad (9)$$

$$\upsilon = \frac{V_L^2 - 2V_T^2}{2(V_L^2 - V_T^2)}, \quad (10)$$

$$E = 2G(1 + \upsilon) \quad (11)$$

III. RESULTS AND DISCUSSION

III.A Boron and aluminum speciation. In the studied glasses, both Al and B can attain different coordination numbers with oxygen, depending on the chemical composition [35,36], as well as thermal and pressure history [23]. Network-forming Al and B cations coordinated with more than three oxygen anions require a network modifier (e.g., alkali cation) to maintain charge-neutrality. An increase in oxygen coordination number manifests itself in larger shielding of the nuclei when probed by MAS NMR spectroscopy, giving rise to additional resolvable signals upfield. The ^{11}B and ^{27}Al MAS NMR spectra (Fig. 1) of the investigated glasses show pronounced differences in the chemical environments for both B and Al. The majority of boron atoms are in three-fold coordination (B^{III}), with some four-coordinated sites (B^{IV}) present as well. Aluminum atoms exist almost exclusively in four-fold coordination (Al^{IV}), with the exception of the Li-glass, which has substantial fractions of five- (Al^{V}) and six-fold coordinated (Al^{VI}) species.

Spectral deconvolution performed using DMFit [32] allows us to extract the relative populations of each site (Table 2), showing that the connectivity of the glasses is sensitive to the *FS* of the network modifier. A local minimum in the average coordination number of boron ($<n_B>$) as a function of *FS* is found for the K-glass (Fig. 2). However, given the experimental error in $<n_B>$ (±0.01) and the discrepancy in the nominal vs. analyzed composition (molar percentage of K_2O is the smallest, Table 1), it is likely that boron speciation is approximately constant at low *FS* and then increases dramatically for the smaller Na- and Li-cations. Similarly, the aluminum speciation is not subject to significant changes as a function of *FS*, with the exception of the Li-glass (Fig. 2). The difference in the structure of the Li-glass compared to the other lower-*FS* glasses could be related to the preference for modifiers to charge-balance Al^{IV} vs. B^{IV} units. That is, in alkali aluminoborate glasses, B and Al tetrahedra compete for the charge-balancing alkali cation, with a well-known preference for alkali-Al^{IV} association [35]. However, previous studies [37,38] suggest that the extent of disorder in oxide glasses increases with increasing *FS*, suggesting a more random association of different network modifiers and formers. As such, our results suggest that the preference for Li^+ to associate with Al^{IV}

over B^{IV} units is low compared with the lower-*FS* glasses. In other words, Li^+ cations appear to be more randomly distributed throughout the network, which explains the large fraction of B^{IV} units for M = Li compared with the other glasses. As a result, a higher fraction of Al-atoms must attain a network-modifying role as Al^V and/or Al^{VI} units.

It should also be noted that the alkali *FS* depends on the glass composition, as the alkali coordination number with oxygen depends on it chemical environment. In turn, the coordination number affects its ionic radius, which is used in the calculation of *FS* (Eq. (1)). In this study, we have assumed the coordination number of all alkali cations to be 6. A detailed structural study would be necessary to determine the actual coordination number for all the studied glasses, but this would be outside the scope of the present study. However, we note that lighter alkali elements tend to have lower coordination numbers, while heavier ones generally display higher coordination numbers [39]. If we consider this in the calculation of *FS*, the differences in *FS* between the five alkali metals would actually increase. As such, the trend presented in Fig. 2 (and in the subsequent figures) remains qualitatively correct despite the assumption of six-fold coordination with oxygen for all alkali ions.

III.B Glass transition temperature and density. The effect of the modifier field strength on the glass transition temperature is illustrated in Fig. 3, revealing an increase in T_g with increasing *FS*. According to the NMR data, substituting Li_2O for Na_2O results in more atomic constraints per atom (higher connectivity), i.e., a more rigid glass network that could result in a higher T_g [40]. However, the network connectivity is not a linear function of *FS* for the lower-*FS* glasses (Fig. 2), i.e., the monotonic increase in T_g with increasing *FS* is not only determined by the average coordination numbers of Al and B. In addition, the difference in the strength of the constraints associated with the alkali-oxygen bonds should be considered [41]. Namely, high-*FS* alkali cations generally form stronger bonds with oxygen [7,42], in agreement with the positive correlation between *FS* and T_g in Fig. 3.

The room temperature density and thus molar volume (V_m) of the as-prepared glasses are also strongly dependent on the alkali oxide added to the aluminoborate network (Table 1). The heavy alkali elements like Cs and Rb are expected to yield a relatively high density glass given their large mass and indeed the density initially decreases with increasing *FS* (Fig. 4). However, as Na_2O is substituted for K_2O, the density

increases despite the fact that Na is lighter than K. This suggests that the observed trend in the density might result from a balance between the atomic weight of the modifiers and the efficiency of their local packing. The atomic packing efficiency increases with the *FS*. Considering the constituent atoms as spheres with a known ionic radius [43], one can determine the atomic packing density (C_g). Assuming 6-fold coordination for all alkali cations, 2-fold coordination for oxygen anions, and 3- to 6-fold coordination for B and Al atoms based on our previous work [23,24], C_g can be calculated as

$$C_g = \frac{\rho \Sigma f_i \left(4/3\pi N \left(x r_A^3 + y r_B^3\right)\right)}{\Sigma f_i M_i}, \quad (12)$$

where for the *i*th constituent with chemical formula A_xB_y, f_i is the molar fraction, r_A and r_B are the ionic radii, M_i is the molar mass, and N is Avogadro's number. C_g is indeed found to increase with increasing modifier *FS* (Fig. 4). The local minimum in density can be explained from the fact that (i) smaller modifiers can more efficiently fill the voids left between O atoms, thereby reducing the amount of internal free volume, and (ii) modifiers exhibiting large *FS* tend to attract more the surrounding O atoms, thereby forcing them to partially overlap with each other. This is consistent with recent molecular dynamics simulations showing that the O atoms around network formers (i.e., *FS* > 1.3 $Å^{-2}$) are experiencing a compressive state due to the strong attraction from the central cation [44].

The observed dependence of T_g and C_g on the modifier field strength therefore suggests that when the low-*FS* Cs_2O modifies the aluminoborate network, the glass is relatively loosely packed and the individual bonds are weak. However, when the high-*FS* Li_2O is used as a modifier, the structure is more rigid and tightly packed with stronger alkali–oxygen bonds.

III.C Hardness and elasticity. Vickers microindentation of the glasses at 19.6 N load results in square-shaped indent impressions in their surfaces, as illustrated in the inset of Fig. 5a. According to Eq. (4), the diagonal lengths (marked by green lines in the inset of Fig. 5a) and the applied load are used to determine the Vickers hardness (H_V), i.e., the glass' resistance to elastoplastic deformation. Increasing the *FS* of the alkali cation has a positive influence on H_V of the aluminoborate glasses as H_V increases from ~2 to ~4 GPa when Li_2O is substituted for Cs_2O (Fig. 5a). A similar trend was recorded for T_g (Fig. 3), implying that both of these properties have similar structural origin (inset of Fig. 3). Indeed, both T_g and H_V have been linked to the

number of atomic constraints per atom, defining the rigidity of the glass network [22,45]. Considering here the lack of a linear increase in coordination numbers of the network-forming cations (B and Al) as a function of increasing *FS* of the alkali cation, we infer that the rigidity of the aluminoborate glasses is sensitive to the modifier constraints. H_V of the glass samples compressed at 1 GPa at their respective ambient pressure T_g values has also been determined (Table 3). In agreement with previous work on pre-densified glasses, H_V increases with increasing applied pressure and thus degree of densification [46]. The magnitude of the hardness increase scales positively with the extent of pressure-induced density increase (Table 3).

In addition to Vickers microindentation, the glasses have also been subjected to depth-sensing instrumented nanoindentation. Eq. (6) is used to compute H_{nano} using the information extracted from the unloading part of the load-displacement curves (see example in the inset of Fig. 5a). The compositional scaling of H_{nano} resembles that of H_V. Nanoindentation also provides insight into the elastic recovery of the glass. By considering the unloading part of the load-displacement curve, the indentation modulus (E_{IT}) can be determined using Eqs. (7)-(9). Similarly to the trends observed for T_g, H_V and H_{nano}, we find a positive linear correlation between E_{IT} and the *FS* of the modifying alkali cation (Fig. 5b).

The compositional trend in E_{IT} is similar to that observed in Young's modulus (E) as measured using the ultrasonic echography method (Fig. 5b). However, the absolute values tend to differ slightly, especially for the low-*FS* alkali glasses. This is likely due to an overestimation of E_{IT}, which is frequently ascribed to formation of pile-up during indentation [47]. The shear modulus (G) exhibits a similar dependence on *FS* as E and E_{IT} (Fig. 5b). We should note that E and G for the Li-glass have been measured using Brillouin scattering [24], i.e., the absolute values for the investigated glasses may not be directly comparable, but the positive correlation between elastic moduli and *FS* is clearly confirmed. Furthermore, the increases in the elastic moduli due to hot compression correspond well to the observed increases in density (Table 3) [48].

In addition to the magnitude of resistance to elastic deformation, the ultrasonic echography method can be used to determine the Poisson's ratio (v), which has been found to be an important metric for understanding the mechanical properties of glasses [49]. For the present alkali aluminoborate glasses, v decreases with increasing *FS* (Fig. 5b). Furthermore, we find that v increases linearly with V_m (Fig. 5c). This suggests that open aluminoborate glass networks exhibit higher v. This is unexpected as there is generally a positive correlation between packing efficiency (C_g) and v when considering different glass systems [8], but

here we observe the opposite trend (inset of Fig. 5c). Materials with a closely packed structure (i.e., high C_g and low V_m) should exhibit small volume changes when changing shape, since there is limited room for densification, which should in turn manifest itself in a high v-value. However, this explanation does not appear to hold for the present aluminoborate glasses. Rouxel [8] has argued that v also depends on the dimensionality of the material, which is dictated by the connectivity. That is, for low-connectivity glasses like amorphous Se, it is easy for the atoms to rearrange upon loading and thus for the material to expand laterally during longitudinal compression. On the other hand, glasses exhibiting high connectivity are more rigid and cannot easily rearrange and will tend to store some internal stress rather than reorganizing on the direction normal to the load. However, considering the NMR data for the studied glasses, the aluminum and boron speciation are roughly constant at low *FS* values (Fig. 2). The trend in connectivity can therefore only partially explain the negative correlation between C_g and v. We thus infer that the unexpected *FS*-dependence of v (Fig. 5b) is a result of the varying strength of the alkali–oxygen bond constraints, which are expected to increase with *FS* along with the increasing dissociation energy of the alkali–oxygen bonds [7,26,42]. Hence, for the alkali aluminoborates studied here, the lowest v values are found in glasses with the weakest bonds, and not in glasses with the highest C_g as shown in other systems [8].

III.D Densification upon hot compression. Next we investigate the glasses' tendency to densify upon hot compression. The extent of densification is quantified through the plastic compressibility (β, Eq. (3)). As shown in Fig. 6a, there is no monotonic correlation between β and *FS*. That is, β exhibits a pronounced minimum around the K-glass. This suggests that two competing deformation mechanisms are at play. The high β-value of the low-*FS* Cs-glass could be due to its relatively low C_g value (Fig. 4), resulting in a large potential for densification achieved by local compaction of the network atoms with only limited changes in the next nearest neighbor environment. In other words, we infer that densification of the low-*FS* glasses is dominated by medium range order reorganization. Upon increasing the *FS* through substitution of K_2O for Cs_2O, C_g also increases (Fig. 4), which likely requires more significant changes in the short range order of the network in order to allow for further compaction of the atoms, thus causing β to decrease initially as a function of *FS*. However, as *FS* increases further when the size of the modifying cation becomes even smaller (i.e., substitution of Li_2O for K_2O), the ability of the cations to charge-stabilize adjacent boron and

aluminum tetrahedra at high pressure is improving given that smaller cations occupy less space around those tetrahedral units [50]. This hypothesis is supported by our previous work concerning the self-adaptivity of the Li- vs- Na-containing aluminoborate glasses [23,24]. More specifically, the pressure-induced increase in the coordination number of both B and Al is higher for the Li-glass compared to the Na-glass, indicating that Li^+ ions enable more permanent densification through structural transformations in the short range order. Hence, we suggest that the increase in β with increasing *FS* is due to the smaller pressure-driven resistance to changes in glass connectivity at high *FS*.

III.E Indentation deformation mechanism. The structural reasoning for the composition dependence of densification upon hot compression suggested above could also hold for that of densification upon sharp contact loading. However, the trend in V_R is opposite that of β (Fig. 6a), suggesting that the Li-glass has a higher resistance to indentation densification. As we discuss in detail below, this may be due to the large differences among the glasses in their elastic response to indentation, which strongly affects the initial indentation volume, V_i^-. We should note that we are not able to correctly determine the V_R value of the Cs-glass, as it exhibits an anelastic response or alternatively corrosion of the indented zone (see Fig. 6b), resulting in an underestimation of V_i^-. The volumes used to calculate V_R for the other glasses are given in Table 4.

To obtain information of the glasses' elastic recovery, we here consider the bow-in of the indent faces upon unloading, which exhibits clear composition dependence. Fig. 7a illustrates the recorded AFM images of the investigated glasses (with the exception of Cs-glass due to the same reason as stated above). By measuring the indent diagonal length (L_D) and the opposite side length (L_S), the elastic response of the material surrounding the indentation-induced cavity can be quantified by calculating the L_D/L_S ratio [51]. We find a negative correlation between L_D/L_S and *FS* (Fig. 7b). As such, the Li-glass has the lowest L_D/L_S ratio and therefore experiences the least elastic recovery during unloading. This is consistent with the trend in elastoplastic ratio *E/H* (inset of Fig. 7b), which also describes the extent of elastic contribution to indentation [52].

The topographic maps of the indent impressions also allow us to estimate the volume fraction of elastic recovery by comparing the post-unloading indentation volume (V_i^-) to the theoretical volume of the

indenter during full loading (V_G). V_G can be calculated from the indent diagonals due to the known geometry of the Vickers pyramid under the assumption that the displacement of corners of the indentation impression during unloading is negligible. The elastic contribution to the total indentation volume (V_E) can then be calculated as $1 - V_i'/V_G$. Using the same approach, we also calculate the densification and shear flow volume fractions (V_D and V_S, respectively) using the volumes determined through AFM experiments (see Fig. 8a and Table 4). V_D is the product of V_R and the V_i'/V_G ratio, while V_S is the remaining volume, i.e., $1 - (V_D + V_E)$. Each of these indent volume contributions are schematically illustrated in Fig. 8b.

By combining the data extracted from AFM, micro-indentation, and ultrasonic echography, we find that both L_D/L_S and V_E exhibit a negative linear scaling with the elastoplastic ratio E/H (Fig. 9). Hence both quantities provide an estimate of the extent of elastic recovery upon unloading of the indenter. For the present series, glasses with higher FS are less prone to recover elastically and thus more of the supplied mechanical energy is dissipated through plastic deformations. Furthermore, we observe that the decreasing elastic recovery coincides with the FS dependence of C_g (Fig. 4), yielding an approximately linear relation between E/H and C_g (inset of Fig. 9). This correlation is in agreement with that found for other glassy solids. For example, amorphous silica with a very open network (i.e., low C_g) displays a relatively pronounced elastic recovery, while densely packed fluoride glasses generally display low extent of elastic recovery [9].

The detailed analysis of the indentation deformation mechanisms described above can be summarized as follows: (i) the extent of elastic recovery is decreasing with increasing FS of the modifier, (ii) the shear flow fraction increases with increasing FS, even though the overall contribution of this deformation mode is small (<18%), and (iii) higher FS facilitates densification. V_R has frequently been used to describe the relative contribution of densification to indentation deformation when comparing different glass compositions [18,33,53–55], and in turn linked to the resistance to indentation cracking. The definition of V_R given in Ref. [33] does not take the elastic recovery into account. As a consequence, glasses with substantial elastic recovery can feature high V_R values due to limited shear flow displacement, but poor resistance to indentation cracking. Hence, we propose that V_D is a more accurate indicator of a glass' ability to dissipate the indentation-induced stress through densification than V_R. For the aluminoborate glasses studied herein, we observe that the Li-glass is in fact the most efficient in relaxing the largest fraction of V_G through densification (Fig. 8), whereas it has the lowest V_R value of the investigated glasses (Fig. 6a), which would

suggest the opposite conclusion. Therefore, when comparing the deformation mechanism among different compositions, the extent of elastic recovery should be considered as it can affect the result of such comparison. We thus suggest considering V_D, and not only V_R, when using AFM studies of indentation imprints to understand the correlation between resistance to indentation cracking and extent of densification.

We also note that the composition dependence of V_D (Fig. 8a) is in good agreement with that of β (Fig. 6a) when considering high-*FS* values, as opposed to V_R. The reason for higher propensity for densification in high-*FS* glasses could be due to the higher ability of the small alkali cations to charge-balance tetrahedral units than the larger cations, as discussed in Section III.A. Alternatively, the increase in connectivity with increasing *FS* (Fig. 2) results in a more efficient "locking" of the deformed zone. This agrees well with molecular dynamic simulations, showing that stressed-rigid glasses exhibit lower elastic recovery compared to isostatic glasses [21,56,57]. In other words, a larger fraction of the volume deformed during loading is deformed irreversibly in glasses with higher connectivity. Although this accounts for the composition dependence of V_D it does not explain why β exhibits a sudden increase with decreasing *FS* when considering the low-*FS* glasses such as Cs and Rb. The difference in these two trends may originate from the difference in densification mechanisms taking place at room temperature and T_g, respectively. Previous work [58] suggests that elevated temperature enables more medium range order rearrangements, whereas this is strongly limited at ambient temperature.

III.F Indentation cracking. Based on findings in previous studies [9,23,53,59], the extent of indentation-induced densification, Poisson's ratio, and plastic compressibility are all expected to be correlated with the extent and type of indentation cracking. Indeed, when examining the dependence on the probability of crack initiation (*CP*) at 19.6 N on the *FS* of the modifying alkali cation, we observe a local maximum around the Na-glass (Fig. 10a). The relative length of the cracks with respect to the indent size (*c/a* ratio), indicative of the material's brittleness [60], exhibits a strong positive correlation with *FS* (Fig. 10a). This suggests that the high-*FS* Li-glass is the most brittle of the investigated glasses, while still being able to resist the same load as the low-*FS* Rb- and Cs-glasses without cracking. Interestingly, the dependences of *CP* and *c/a* on *FS* appear to be parallel for all glasses except that with Li, as there is a sharp decrease in *CP* from the Na- to the Li-glass. We have also examined the indentation cracking behavior of the compressed glasses. The glasses

become less crack-resistant and more brittle (i.e., displaying higher *c/a*-values) upon hot compression (Table 5), which is in good agreement with previous work [46] and is presumably due to a decreased ability to densify further during indentation following pre-densification [61].

Next we combine the information from indentation (crack length and hardness at given load) and ultrasonic echography (elastic modulus) to calculate the indentation fracture toughness (K_{Ic}) for the studied series of glasses. It should be noted that indentation testing is not a valid method to calculate fracture toughness, which is a material property [62], and the empricial values of indentation fracture toughness should therefore be treated with caution. That is, the K_{Ic} values are not necessarily comparable with toughness values obtained through self-consistent methods [63]. This is especially true in the case of the present glasses, which experience significant densification during indentation [64]. However, for the sake of internal comparison, we use indentation testing to estimate the toughness of these glasses. Depending on the *c/a* ratio, one should select the appropriate equation for calculating K_{Ic}. The equation suggested by Anstis [65], (Eq. (13)), should be used if *c/a*>2.5, and the Niihara equation [66], (Eq. (14)), otherwise. The difference in equations is meant to capture the difference in cracking systems, where Eq. (13) is suitable for fully connected median/radial cracks originating below the center of the indent, while Eq. (14) is used for Palmqvist cracks emanating from the corners of the indent [67].

$$K_{Ic}^{Ans} = 0.016\left(\frac{E}{H}\right)^{0.5}\frac{P}{c^{1.5}} \quad (13)$$

$$K_{Ic}^{Nii} = 0.018H^{0.6}E^{0.4}a(c-a)^{-0.5} \quad (14)$$

For the present glasses, the selection of the appropriate K_{Ic} equation based on the *c/a* value is complicated by the fact that the low-*FS* glasses exhibit *c/a* < 2.5, whereas the high-*FS* glasses exhibit *c/a* > 2.5 (Fig. 10a). Therefore, we subject the glasses to mild surface polishing subsequent to indentation in order to look into the type of cracks formed during indentation. The cracks emanating from the corners of the indent are radial in every case, as shown in the image of an indent produced at 19.6 N in the Na-containing glass (Fig. 10b). This is also found for the other compositions studied herein (images not shown). The fact that the cracks are not connected to the corners of the indent beneath the original surface strongly suggests that the cracking system is of Palmqvist type. This agrees with the expected type of cracking based on Yoffe's indentation stress field [68]. Sellapan *et al.* [9] calculated that there should be no driving force for ring and median indentation

cracking at this set of *v*- and *E/H*-values, while lateral and radial cracking should be expected. Hence, we apply Eq. (14) to calculate the indentation fracture toughness. We observe a minimum in K_{Ic} for intermediate *FS*-values (Fig. 11a). We note that the trend in K_{Ic} correlates inversely with that in *CP* (Fig. 10a), indicating that the ability to withstand indentation cracking is correlated to the critical stress intensity for crack propagation within this system, although no one-to-one correlation is observed (not shown). Moreover, we observe that the minimum in K_{Ic} coincides with that in β (Fig. 6a), yielding an approximate positive linear correlation among these two properties (Fig. 11b). This suggests that K_{Ic} is controlled by the atomic self-adaptivity introduced in our previous paper [24]. Alternatively, the origin of the minimum in K_{Ic} is the competition between two effects: (i) decreasing brittleness with increasing *FS*, in agreement with the trend in *c/a* value (Fig. 10a), and (ii) increasing fracture surface energy with increasing *FS* due to stronger alkali–oxygen bonds [69].

IV. CONCLUSIONS

We have probed the densification behavior and mechanical properties for a series of slightly peralkaline alkali aluminoborate glasses with varying field strength of the modifying alkali cation. Substitution of the alkali oxide in the glassy network manifests itself in a linear increase in glass transition temperature, hardness and elastic moduli with increasing field strength, which is explained by the stronger alkali–oxygen bonds. We find that Poisson's ratio surprisingly scales negatively with the atomic packing density, which might be ascribed to the bond strength and the trend in network connectivity. The ratio between densified volume and permanently displaced total indentation volume exhibits a maximum at intermediate modifier field strength, whereas the ratio between densified volume and full geometrical indentation volume shows a linear increase as a function of field strength. This difference in trends shows the importance of considering the elastic recovery during indenter unloading, inferring that the latter ratio is a more appropriate measure of densification resistance. That is, high modifier field strength glasses are found to exhibit lower resistance to densification, thus dissipating stresses more easily. The indentation fracture toughness displays a minimum at intermediate modifier field strength, which coincides with that found in the extent of densification during hot compression. We suggest that the fracture toughness of the aluminoborate glasses is correlated with the

glass' ability to undergo densification-facilitating structural transformations when subjected to pressure, thus dissipating residual stress during indentation.

ACKNOWLEDGEMENTS

The authors thank Yuanwei Chang (University of California, Los Angeles) for technical assistance with nanoindentation measurements, Vladimir Popok (Aalborg University) for access to the atomic force microscope, and Ashutosh Goel (Rutgers University) for valuable discussions. K.J. and M.M.S. acknowledge financial support from VILLUM FONDEN under research grant no. 13253. M.Bauchy acknowledges financial support from the National Science Foundation under Grant No. 1562066. S.J.R. acknowledges financial support from the National Science Center of Poland under Grant No. UMO-2016/21/B/ST3/02203. The purchase of the ultrasonic thickness gauge was supported by the Obel Family Foundation.

REFERENCES

[1] C. R. Kurkjian, P. K. Gupta, R. K. Brow, and N. Lower, J. Non. Cryst. Solids **316**, 114 (2003).

[2] A. A. Griffith, Math. or Phys. Character **221**, 163 (1921).

[3] F. Célarie, S. Prades, D. Bonamy, L. Ferrero, E. Bouchaud, C. Guillot, and C. Marlière, Phys. Rev. Lett. **90**, 75504 (2003).

[4] B. Wang, Y. Yu, M. Wang, J. C. Mauro, and M. Bauchy, Phys. Rev. B **93**, 64202 (2016).

[5] M. M. Smedskjaer, C. Hermansen, and R. E. Youngman, MRS Bull. **42**, 29 (2017).

[6] E. D. Zanotto and F. A. B. Coutinho, J. Non. Cryst. Solids **347**, 285 (2004).

[7] A. Makishima and J. D. Mackenzie, J. Non. Cryst. Solids **12**, 35 (1973).

[8] T. Rouxel, J. Am. Ceram. Soc. **90**, 3019 (2007).

[9] P. Sellappan, T. Rouxel, F. Celarie, E. Becker, P. Houizot, and R. Conradt, Acta Mater. **61**, 5949 (2013).

[10] A. Arora, D. B. Marshall, B. R. Lawn, and M. V. Swain, J. Non. Cryst. Solids **31**, 415 (1979).

[11] J. T. Hagan, J. Mater. Sci. **14**, 462 (1979).

[12] K. W. Peter, J. Non. Cryst. Solids **5**, 103 (1970).

[13] D. Wakabayashi, N. Funamori, and T. Sato, Phys. Rev. B **91**, 14106 (2015).

[14] V. Keryvin, L. Charleux, R. Hin, J.-P. Guin, and J.-C. Sangleboeuf, Acta Mater. **129**, 492 (2017).

[15] J. Luo, P. J. Lezzi, K. D. Vargheese, A. Tandia, J. T. Harris, T. M. Gross, and J. C. Mauro, Front. Mater. **3**, 52 (2016).

[16] S. Striepe, M. M. Smedskjaer, J. Deubener, U. Bauer, H. Behrens, M. Potuzak, R. E. Youngman, J. C. Mauro, and Y. Yue, J. Non. Cryst. Solids **364**, 44 (2013).

[17] S. Yoshida, J. Matsuoka, and N. Soga, J. Non. Cryst. Solids **316**, 28 (2003).

[18] M. Barlet, J.-M. Delaye, T. Charpentier, M. Gennison, D. Bonamy, T. Rouxel, and C. L. Rountree, J. Non. Cryst. Solids **417**, 66 (2015).

[19] L. Wondraczek, J. C. Mauro, J. Eckert, U. Kühn, J. Horbach, J. Deubener, and T. Rouxel, Adv. Mater. **23**, 4578 (2011).

[20] J. C. Mauro, Front. Mater. **1**, 20 (2014).

[21] M. Bauchy, B. Wang, M. Wang, Y. Yu, M. J. A. Qomi, M. M. Smedskjaer, C. Bichara, F.-J. Ulm, and R. Pellenq, Acta Mater. **121**, 234 (2016).

[22] M. M. Smedskjaer, J. C. Mauro, and Y. Yue, Phys. Rev. Lett. **105**, 115503 (2010).

[23] K. Januchta, R. E. Youngman, A. Goel, M. Bauchy, S. J. Rzoska, M. Bockowski, and M. M. Smedskjaer, J. Non. Cryst. Solids **460**, 54 (2017).

[24] K. Januchta, R. E. Youngman, A. Goel, M. Bauchy, S. L. Logunov, S. J. Rzoska, M. Bockowski, L. R. Jensen, and M. M. Smedskjaer, Chem. Mater. (2017).

[25] A. Dietzel, Zeitschrift Für Elektrochemie Und Angew. Phys. Chemie **48**, 9 (1942).

[26] A. K. Varshneya, *Fundamentals of Inorganic Glasses* (Elsevier, 2013).

[27] M. Yamane and J. . Mackenzie, J. Non. Cryst. Solids **15**, 153 (1974).

[28] C. Weigel, C. Le Losq, R. Vialla, C. Dupas, S. Clément, D. R. Neuville, and B. Rufflé, J. Non. Cryst. Solids **447**, 267 (2016).

[29] M. Tiegel, R. Hosseinabadi, S. Kuhn, A. Herrmann, and C. Rüssel, Ceram. Int. **41**, 7267 (2015).

[30] G. Kaur, O. P. Pandey, and K. Singh, J. Non. Cryst. Solids **358**, 2589 (2012).

[31] M. M. Smedskjaer, S. J. Rzoska, M. Bockowski, and J. C. Mauro, J. Chem. Phys. **140**, 54511 (2014).

[32] D. Massiot, F. Fayon, M. Capron, I. King, S. Le Calvé, B. Alonso, J.-O. Duran, B. Bujoli, Z. Gan, and G. Hoatson, Magn. Reson. Chem. **40**, 70 (2002).

[33] S. Yoshida, J.-C. Sanglebœuf, and T. Rouxel, J. Mater. Res. **20**, 3404 (2005).

[34] W. C. Oliver and G. M. Pharr, J. Mater. Res. **7**, 1564 (1992).

[35] L. Züchner, J. C. C. Chan, W. Müller-Warmuth, and H. Eckert, J. Phys. Chem. B **102**, 4495 (1998).

[36] L.-S. Du and J. F. Stebbins, Solid State Nucl. Magn. Reson. **27**, 37 (2005).

[37] H. Maekawa, T. Maekawa, K. Kawamura, and T. Yokokawa, J. Non. Cryst. Solids **127**, 53 (1991).

[38] S. K. Lee and J. F. Stebbins, J. Phys. Chem. B **104**, 4091 (2000).

[39] E. I. Kamitsos and G. D. Chryssikos, Solid State Ionics **105**, 75 (1998).

[40] M. Micolaut and G. G. Naumis, Europhys. Lett. **47**, 568 (1999).

[41] C. Hermansen, B. P. Rodrigues, L. Wondraczek, and Y. Yue, J. Chem. Phys. **141**, 244502 (2015).

[42] K.-H. Sun, J. Am. Ceram. Soc. **30**, 277 (1947).

[43] R. D. Shannon, Acta Crystallogr. Sect. A **32**, 751 (1976).

[44] B. Wang, N. M. A. Krishnan, Y. Yu, M. Wang, Y. Le Pape, G. Sant, and M. Bauchy, J. Non. Cryst. Solids **463**, 25 (2017).

[45] J. C. Mauro, P. K. Gupta, and R. J. Loucks, J. Chem. Phys. **130**, 234503 (2009).

[46] S. Kapoor, L. Wondraczek, and M. M. Smedskjaer, Front. Mater. **4**, 1 (2017).

[47] Q. Zhao, M. Guerette, and L. Huang, J. Non. Cryst. Solids **358**, 652 (2012).

[48] M. N. Svenson, M. Guerette, L. Huang, N. Lönnroth, J. C. Mauro, S. J. Rzoska, M. Bockowski, and M. M. Smedskjaer, Chem. Phys. Lett. **651**, 88 (2016).

[49] G. N. Greaves, A. L. Greer, R. S. Lakes, and T. Rouxel, Nat. Mater. **10**, 823 (2011).

[50] J. Wu and J. F. Stebbins, J. Non. Cryst. Solids **355**, 556 (2009).

[51] S. Yoshida, M. Kato, A. Yokota, S. Sasaki, A. Yamada, J. Matsuoka, N. Soga, and C. R. Kurkjian, J. Mater. Res. **30**, 2291 (2015).

[52] B. R. Lawn and V. R. Howes, J. Mater. Sci. **16**, 2745 (1981).

[53] Y. Kato, H. Yamazaki, S. Yoshida, and J. Matsuoka, J. Non. Cryst. Solids **356**, 1768 (2010).

[54] C. Hermansen, J. Matsuoka, S. Yoshida, H. Yamazaki, Y. Kato, and Y. Z. Yue, J. Non. Cryst. Solids **364**, 40 (2013).

[55] R. Limbach, A. Winterstein-Beckmann, J. Dellith, D. Möncke, and L. Wondraczek, J. Non. Cryst. Solids **417**–**418**, 15 (2015).

[56] J. C. Mauro and A. K. Varshneya, J. Am. Ceram. Soc. **90**, 192 (2007).

[57] M. Bauchy, M. Wang, Y. Yu, B. Wang, N. M. A. Krishnan, F.-J. Ulm, and R. Pellenq, Phys. Rev. Lett. **119**, 35502 (2017).

[58] M. Guerette, M. R. Ackerson, J. Thomas, F. Yuan, E. B. Watson, D. Walker, and L. Huang, Sci. Rep. **5**, 15343 (2015).

[59] T. M. Gross, J. Non. Cryst. Solids **358**, 3445 (2012).

[60] J. Seghal and S. Ito, J. Am. Ceram. Soc. **81**, 2485 (1998).

[61] K. G. Aakermann, K. Januchta, J. A. L. Pedersen, M. N. Svenson, S. J. Rzoska, M. Bockowski, J. C. Mauro, M. Guerette, L. Huang, and M. M. Smedskjaer, J. Non. Cryst. Solids **426**, (2015).

[62] G. D. Quinn and R. C. Bradt, J. Am. Ceram. Soc. **90**, 673 (2007).

[63] T. Rouxel and S. Yoshida, J. Am. Ceram. Soc. (2017).

[64] S. S. Chiang, D. B. Marshall, and A. G. Evans, J. Appl. Phys. **53**, 298 (1982).

[65] G. R. Anstis, P. Chantikul, B. R. Lawn, and D. B. Marshall, J. Am. Ceram. Soc. **64**, 533 (1981).

[66] K. Niihara, R. Morena, and D. P. H. Hasselman, J. Mater. Sci. Lett. **1**, 13 (1982).

[67] C. B. Ponton and R. D. Rawlings, Mater. Sci. Technol. **5**, 865 (1989).

[68] E. H. Yoffe, Philos. Mag. A **46**, 617 (1982).

[69] T. Rouxel, Scr. Mater. **137**, 109 (2017).

Table 1. Analyzed chemical compositions, glass transition temperature (T_g), density (ρ), molar volume (V_m), and atomic packing density (C_g) of the as-prepared glasses. The plastic compressibility (β) following hot compression is also given. The errors in T_g, ρ, V_m, C_g, and β do not exceed ± 2 °C, ± 0.001 g/cm^3, ± 0.02 cm^3/mol, ± 0.001, and ± 0.002 GPa^{-1}, respectively.

Glass-ID	$[M_2O]$ (mol%)	$[Al_2O_3]$ (mol%)	$[B_2O_3]$ (mol%)	T_g (°C)	ρ (g/cm^3)	V_m (cm^3/mol)	C_g (-)	B (GPa^{-1})
Li[a]	24.1	20.9	55.1	478	2.241	29.52	0.545	0.081
Na[b]	25.5	20.4	54.1	451	2.240	33.11	0.510	0.061
K	22.8	21.7	55.5	429	2.170	37.90	0.498	0.054
Rb	24.0	20.7	55.3	417	2.595	40.63	0.492	0.058
Cs	24.8	19.9	55.3	416	2.886	44.75	0.479	0.072

[a] Data are taken from Ref. [24]
[b] Data are taken from Ref. [23]

Table 2. Fractions of three- and four-coordinated boron species (B^{III} and B^{IV}), as well as four-, five-, and six-coordinated aluminum species (Al^{IV}, Al^{V} and Al^{VI}, respectively) determined from MAS NMR experiments. The errors in fractions do not exceed 1 % and 2 % for boron and aluminum fractions, respectively.

Glass-ID	B^{III} (%)	B^{IV} (%)	Al^{IV} (%)	Al^{V} (%)	Al^{VI} (%)
Li[a]	84	16	73	23	4
Na	88	12	97	3	0
K	94	6	95	4	1
Rb	92	8	95	4	1
Cs	92	8	97	1	2

[a] Data are taken from Ref. [24]

Table 3. Vickers hardness at 19.6 N (H_V), nanohardness (H_{nano}), indentation modulus (E_{IT}), Young's modulus (E), shear modulus (G), and Poisson's ratio (v) of the as-prepared and hot compressed (at 1 GPa) glasses. The errors in H_V, H_{nano}, E_{IT}, E, G and v do not exceed ± 0.1 GPa, 0.2 GPa, 2 GPa, 2 GPa, 1 GPa, and 0.015 respectively.

Glass-ID	H_V (GPa)	H_{nano} (GPa)	E_{IT} (GPa)	E (GPa)	G (GPa)	v (-)	H_V (GPa)	H_{nano} (GPa)	E_{IT} (GPa)	E (GPa)	G (GPa)	v (-)
	As-prepared						Compressed					
Li[a]	4.1	5.3	74	69	27	0.281	5.9	7.6	99	90	35	0.274
Na[b]	3.1	3.4	49	43	17	0.291	4.1	4.4	64	55	22	0.286
K	2.4	2.6	34	29	11	0.307	3.3	nd	nd	38	15	0.297
Rb	2.3	2.5	30	24	9	0.314	3.0	nd	nd	32	12	0.307
Cs	2.0	2.2	27	20	8	0.326	2.8	nd	nd	27	10	0.319

[a] All data are taken from Ref. [24]
[b] H_V, H_{nano} and E_{IT} data are taken from Ref. [23]

Table 4. Indentation and pile-up volumes (V_i^- and V_i^+, respectively) for the initial indent, the corresponding volumes after thermal relaxation (V_a^- and V_a^+), volume recovery ratio (V_R), elastic, densification and shear flow volume contributions to full geometrical volume (V_E, V_D, and V_S, respectively), and ratio of indent diagonal length to the opposite side length (L_D/L_S) for the as-prepared glasses. The errors for V_i^-, V_i^+, V_a^-, V_a^+, V_E, V_D, V_S and L_D/L_S do not exceed 0.8 μm^3, 0.6 μm^3, 0.4 μm^3, 0.6 μm^3, 5 %, 4 %, 3 %, 2 %, and 0.04, respectively.

Glass-ID	V_i^- (μm^3)	V_i^+ (μm^3)	V_a^- (μm^3)	V_a^+ (μm^3)	V_R (%)	V_E (%)	V_D (%)	V_S (%)	L_D/L_S (-)
Li[a]	13.4	1.2	5.2	2.2	69	42	40	18	1.65
Na[b]	14.1	1.4	3.9	2.5	80	60	32	8	1.72
K	16.2	1.7	4.7	3.6	83	69	26	5	1.82
Rb	15.0	2.5	4.4	2.9	74	74	20	6	1.90

[a] Data are taken from Ref. [24]
[b] Data are taken from Ref . [23]

Table 5. Crack probability (*CP*), crack to half-diagonal length ratio (*c/a*), and indentation fracture toughness calculated according to Eq. (14) (K_{Ic}) for as-prepared and compressed glasses measured at at 19.6 N indentation load. The estimated errors in *CP*, *c/a*, and K_{Ic} do not exceed ± 5 %, 0.12, and 0.06 MPa m$^{1/2}$, respectively.

Glass-ID	*CP* (%)	*c/a* (-)	K_{Ic} (MPa m$^{1/2}$)	*CP* (%)	*c/a* (-)
	As-prepared			Compressed	
Li[a]	5	2.70	1.26	100	3.54
Na[b]	54	2.62	0.96	99	2.90
K	27	2.02	0.95	88	2.50
Rb	2	1.90	0.94	79	2.81
Cs	5	1.48	1.13	56	2.18

[a] *CP* and *c/a* data are taken from Ref. [24]
[b] *CP* and *c/a* data are taken from Ref. [23]

Figure 1. (a) ^{11}B and (b) ^{27}Al MAS NMR spectra for the investigated glasses. Data for Li- are taken from Ref. [24]. The small peak marked by * is due to background signal from the zirconia rotor.

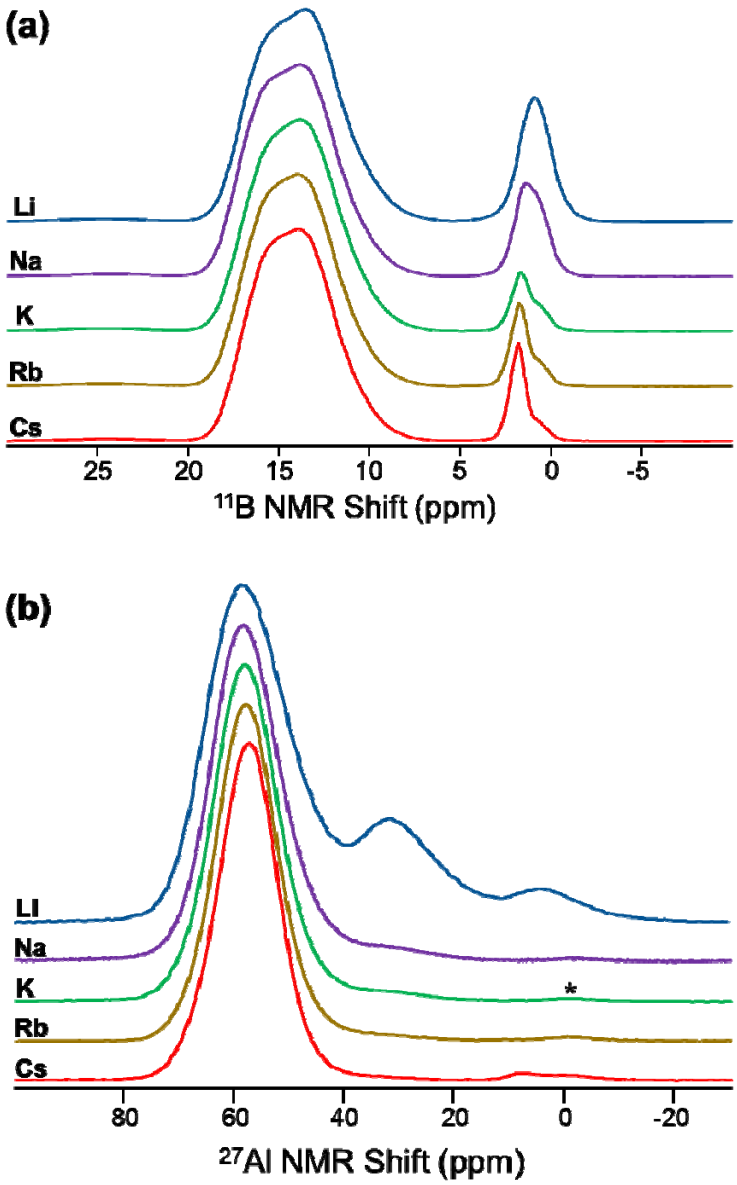

Figure 2. Alkali field strength (*FS*) dependence of the average B coordination number (<n_B>, green triangles) and Al coordination number (<n_{Al}>, blue squares). Data for Li-glass are taken from Ref. [24]. The errors in <n_B> and <n_{Al}> do not exceed 0.01 and 0.02, respectively.

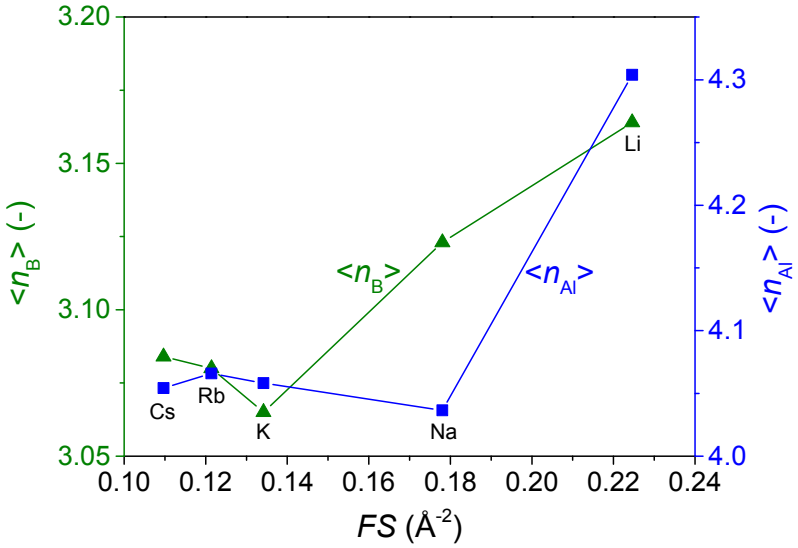

Figure 3. Alkali field strength (*FS*) dependence of the glass transition temperature (T_g). Data for Li- and Na-glasses are taken from Refs. [23,24]. Inset: correlation between T_g and Vickers hardness (H_V). The errors in T_g and H_V do not exceed ±2 °C and ±0.1 GPa, respectively.

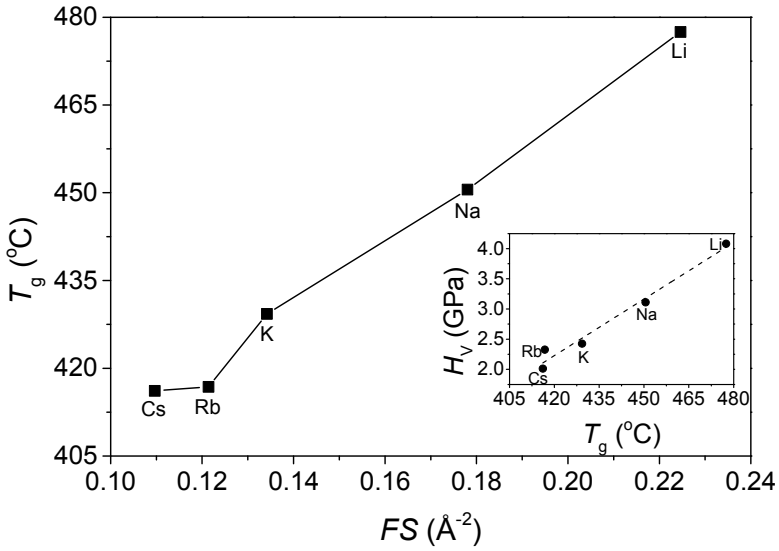

Figure 4. Alkali field strength (*FS*) dependence of density (ρ, green squares) and atomic packing density (C_g, blue triangles). Data for Li- and Na-glasses are taken from Refs. [23,24]. The errors in ρ and C_g are smaller than the size of the symbols.

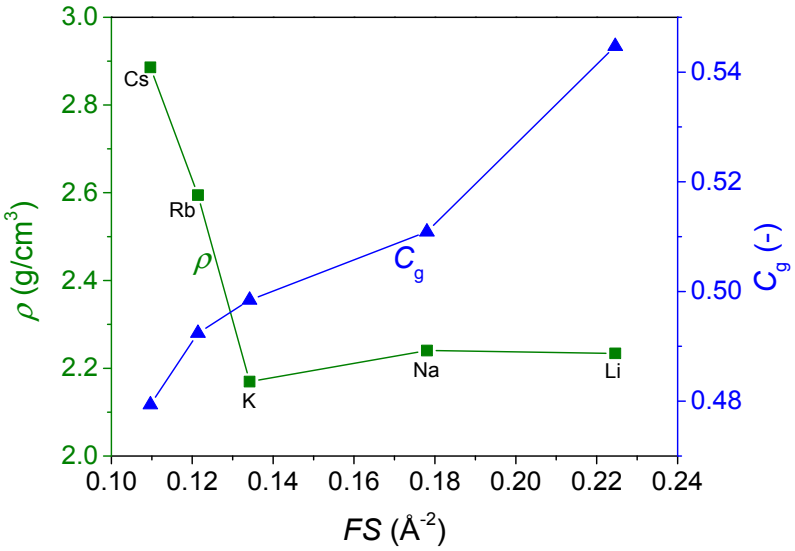

Figure 5. (a) Alkali field strength (*FS*) dependence of Vickers hardness (H_V, black squares) and nanohardness (H_{nano}, blue triangles). Insets: load-displacement curve extracted from nanoindentation and optical microscopy image of a Vicker's indent used to calculate H_{nano} (Eq. (6)) and H_V (Eq. (4)), respectively. (b) *FS* dependence of Young's modulus (*E*, black squares), shear modulus (*G*, green circles), indentation modulus (E_{IT}, blue triangles), and Poisson's ratio (*v*, grey diamonds). (c) Correlation between *v* and molar volume (V_m) and C_g (inset). Data for Li- and Na-glasses are taken from Refs. [23,24]. Errors in H_{nano}, H_V, *E*, *G*, E_{IT}, and *v* do not exceed 0. 2 GPa, 0.1 GPa, 2 GPa, 1 GPa, 2 GPa, and 0.015 respectively.

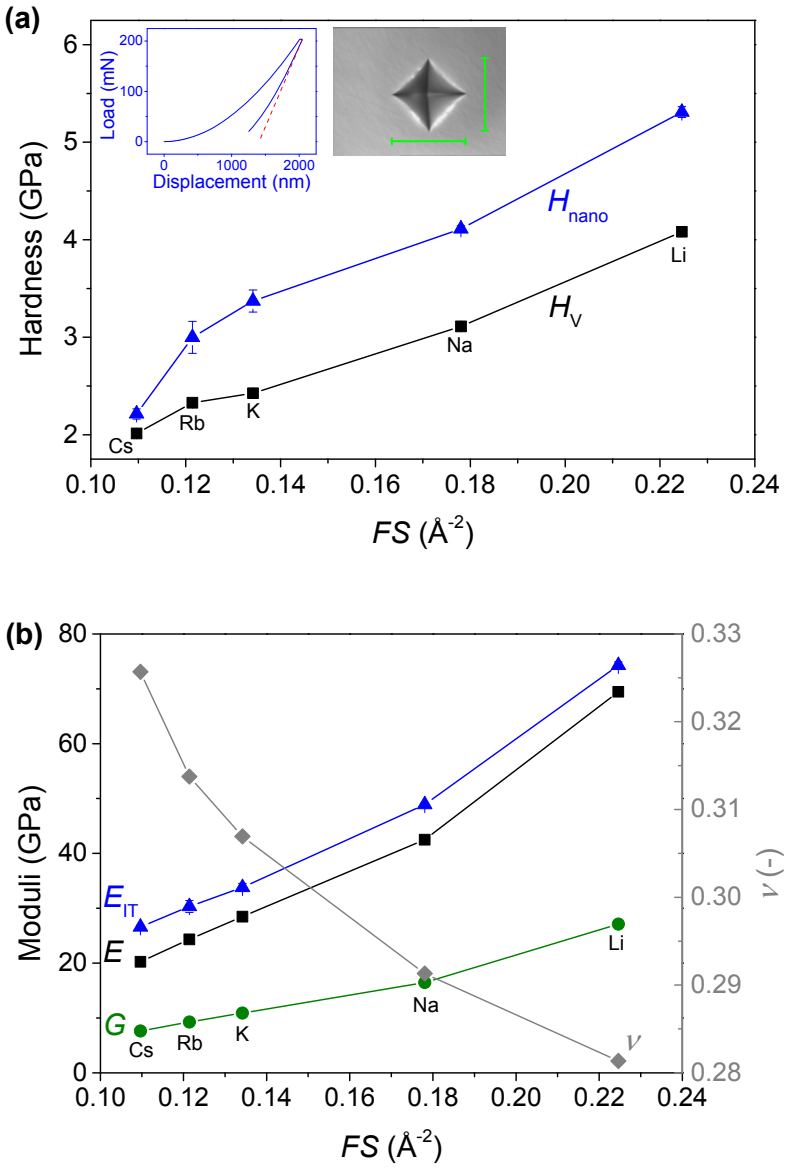

(*Figure 5 continued*)

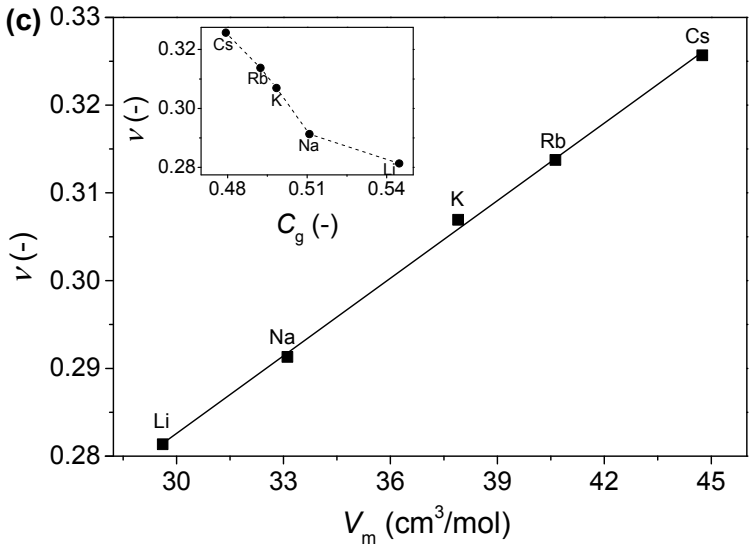

Figure 6. (a) Alkali field strength (*FS*) dependence of volume recovery ratio (V_R, green squares) and plastic compressibility (β, blue triangles). V_R of the Cs-glass could not be determined as explained in the text. Data for Li- and Na-glasses are taken from Refs. [23,24]. (b) Indentation imprint at 0.98 N in the Cs-glass recorded immediately after unloading or after exposure to ambient atmosphere for 2 and 15 h.

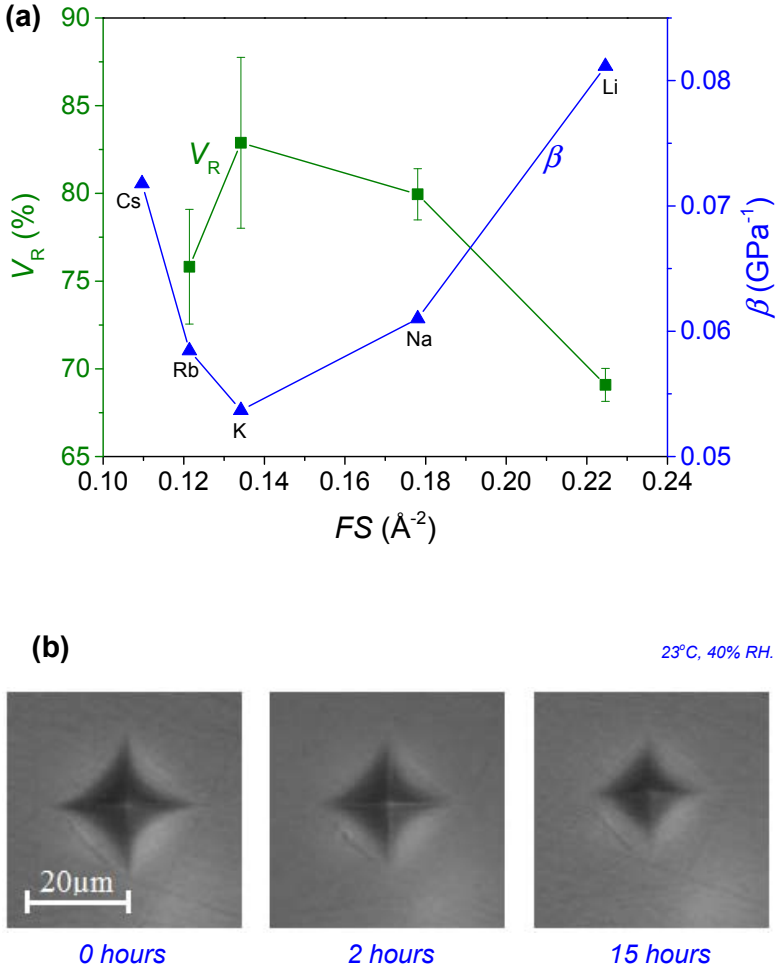

Figure 7. (a) Atomic force microscopy images of indentation imprints produced at 0.25 N in Li-, Na-, K-, and Rb-glasses. The determination of the diagonal length (L_D) and the opposite side length (L_S) is illustrated. (b) Alkali field strength (*FS*) dependence of the bow-in parameter L_D/L_S. The dashed line represents the theoretical minimum L_D/L_S value (i.e., the case with no bow-in). Inset: *FS*-dependence of the elastoplastic ratio (*E/H*).

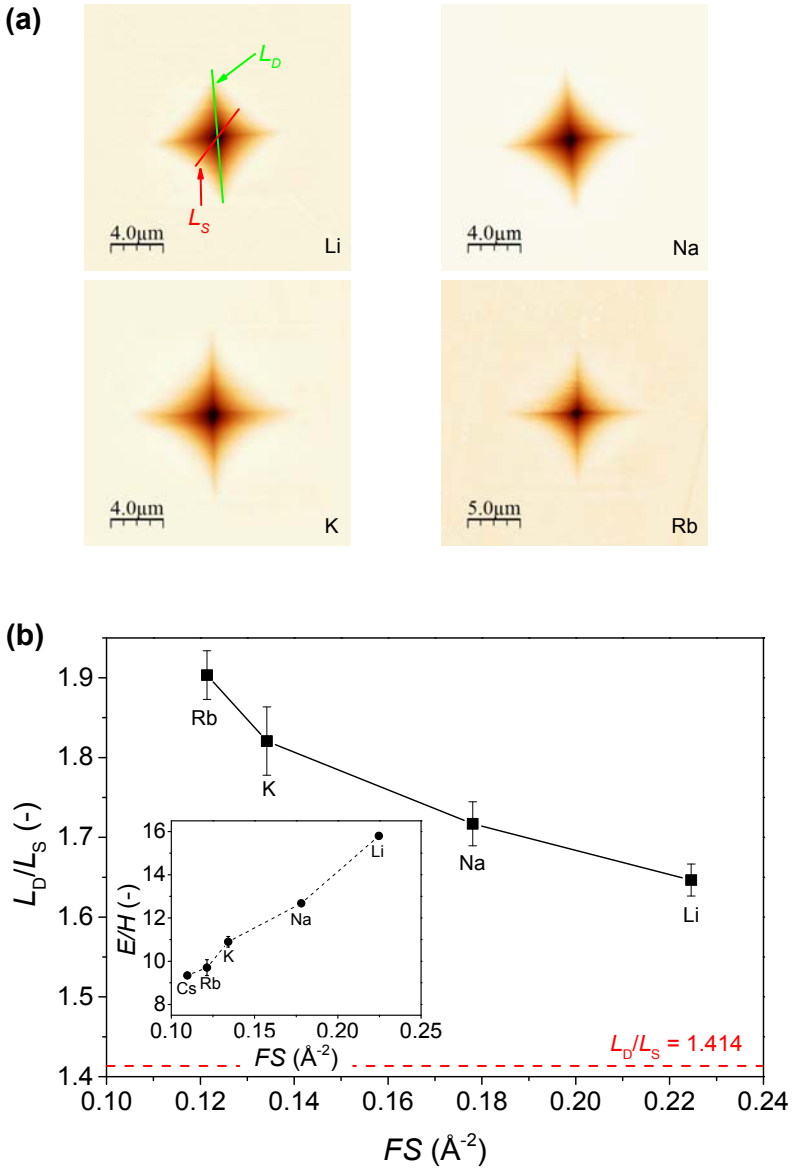

Figure 8. (a) Alkali field strength (*FS*) dependence of the elastic (V_E, blue triangles), densification (V_D, green circles) and shear flow (V_S, black squares) volume fractions determined using AFM. (b) Schematic illustration of how V_E (blue) and V_D (green) are determined. V_S is the remaining volume fraction.

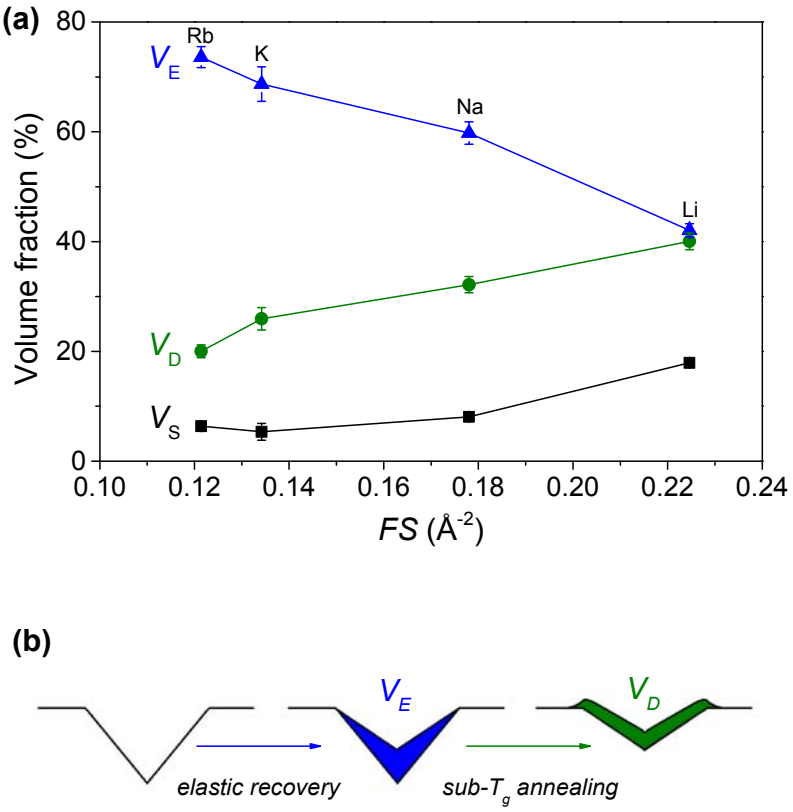

Figure 9. Dependence of the L_D/L_S ratio (blue squares) and the elastic volume fraction (V_E, green triangles) on the elastoplastic ratio (E/H). Inset: correlation between E/H and atomic packing density (C_g).

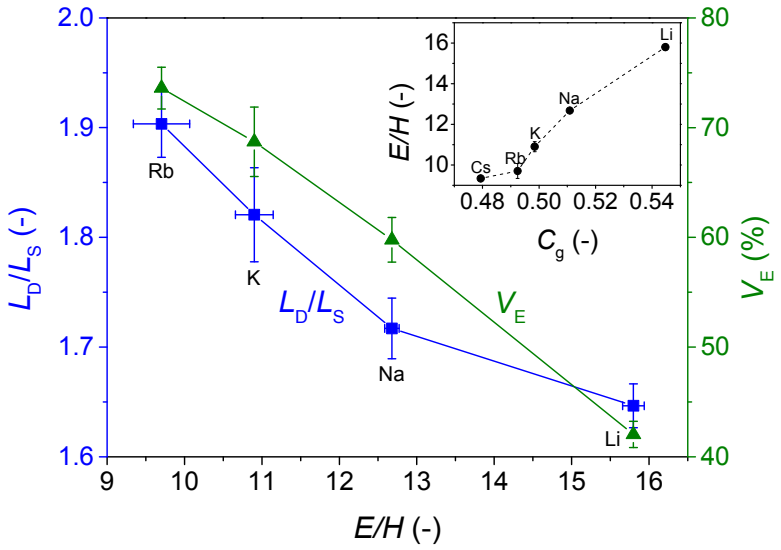

Figure 10. (a) Alkali field strength (*FS*) dependence of the crack probability (*CP*, green squares) and crack-to-indent size ratio (*c/a*, blue triangles) at 19.6 N indentation load. Data for Li- and Na-glasses are taken from Refs. [23,24]. (b) Image of an indent produced at 19.6 N in the Na-glass before (left) and after (right) polishing. The radial cracks emanating from the corners of the indent are not connected to the corners of the indent after removal of the original surface. Since there are residual tensile stresses in the vicinity of the non-cracked corners of the indent, new cracks appear upon polishing.

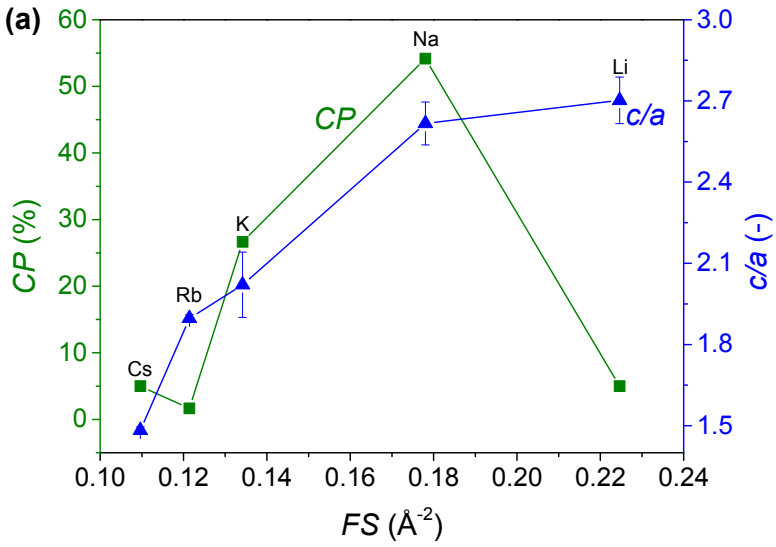

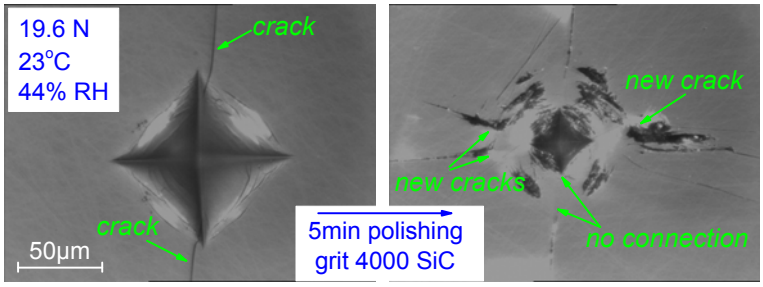

Figure 11. (a) Alkali field strength (*FS*) dependence of indentation fracture toughness (K_{Ic}) calculated by Niihara's equation (Eq. (14)). (b) Correlation between K_{Ic} and plastic compressibility (β). Errors in K_{Ic} and β do not exceed 0.06 MPa $m^{0.5}$ and 0.002 GPa^{-1}, respectively.